

Article

Electrocatalytic Reduction of CO₂ to CO by Molecular Cobalt–Polypyridine Diamine Complexes

Yong Yang ^{1,*}, Fang Xie ^{1,†}, Jiahui Chen ¹, Si Qiu ¹, Na Qiang ¹, Ming Lu ¹, Zhongli Peng ¹, Jing Yang ^{2,*} and Guocong Liu ¹

- ¹ School of Chemistry and Materials Engineering, Huizhou University, Huizhou 516001, China; xiefang4498@126.com (F.X.); cc15363451419@163.com (J.C.); qiusi0206@gmail.com (S.Q.); qiangna93@163.com (N.Q.); reggi_lu@hzu.edu.cn (M.L.); zsupzl@126.com (Z.P.); gcl_109@hzu.edu.cn (G.L.)
- ² College of Health Science and Environmental Engineering, Shenzhen Technology University, Shenzhen 518118, China
- * Correspondence: yangyongself@hzu.edu.cn (Y.Y.); yangjing2@sztu.edu.cn (J.Y.)
- † These authors contributed equally to this work.

Abstract: Cobalt complexes have previously been reported to exhibit high faradaic efficiency in reducing CO₂ to CO. Herein, we synthesized capsule-like cobalt–polypyridine diamine complexes [Co(L¹)](BF₄)₂ (**1**) and [Co(L²)(CH₃CN)](BF₄)₂ (**2**) as catalysts for the electrocatalytic reduction of CO₂. Under catalytic conditions, complexes **1** and **2** demonstrated the electrocatalytic reduction of CO₂ to CO in the presence or absence of CH₃OH as a proton source. Experimental and computational studies revealed that complexes **1** and **2** undergo two consecutive reversible one-electron reductions on the cobalt core, followed by the addition of CO₂ to form a metallocarboxylate intermediate [Co^{II}(L)–CO₂²⁻]⁰. This crucial reaction intermediate, which governs the catalytic cycle, was successfully detected using high resolution mass spectrometry (HRMS). In situ Fourier-transform infrared spectrometer (FTIR) analysis showed that methanol can enhance the rate of carbon–oxygen bond cleavage of the metallocarboxylate intermediate. DFT studies on [Co^{II}(L)–CO₂²⁻]⁰ have suggested that the doubly reduced species attacks CO₂ on the C atom through the d_{z²} orbital, while the interaction with CO₂ is further stabilized by the π interaction between the metal d_{xz} or d_{xz} orbital with p orbitals on the O atoms. Further reductions generate a metal carbonyl intermediate [Co^I(L)–CO]⁺, which ultimately releases CO.

Keywords: cobalt; molecular catalyst; electrocatalysis; CO₂ reduction



Citation: Yang, Y.; Xie, F.; Chen, J.; Qiu, S.; Qiang, N.; Lu, M.; Peng, Z.; Yang, J.; Liu, G. Electrocatalytic Reduction of CO₂ to CO by Molecular Cobalt–Polypyridine Diamine Complexes. *Molecules* **2024**, *29*, 1694. <https://doi.org/10.3390/molecules29081694>

Academic Editor: Wolfgang Weigand

Received: 8 March 2024

Revised: 2 April 2024

Accepted: 8 April 2024

Published: 9 April 2024



Copyright: © 2024 by the authors. Licensee MDPI, Basel, Switzerland. This article is an open access article distributed under the terms and conditions of the Creative Commons Attribution (CC BY) license (<https://creativecommons.org/licenses/by/4.0/>).

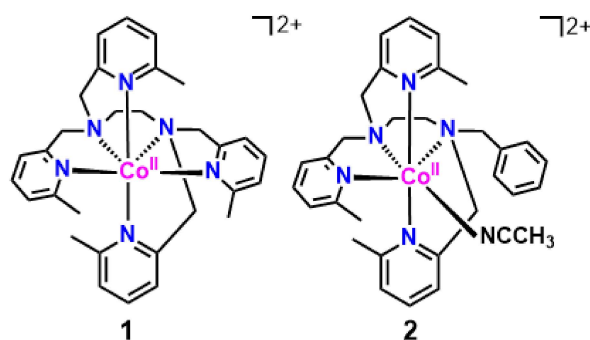
1. Introduction

The transformation of carbon dioxide (CO₂) to fuels and commodity chemicals is one of the most attractive methods to satisfy the energy demand and decrease atmospheric CO₂ levels [1,2]. Electrochemical reduction of CO₂ provides a sustainable approach to achieve this goal [3–6]. However, the electrochemical conversion of CO₂ often faces challenges due to the inherent stability of CO₂, which hinders efficient implementation [7,8]. In nature, the CO-dehydrogenase (CODH) enzyme, containing multi-metallic (Ni, Fe) active sites, is able to convert CO₂ equivalents into CO efficiently [9]. In the active site of CODH, there is a [Ni-4Fe-5S] cluster and the Ni center is the redox active center to which CO₂ binds. Therefore, numerous studies have focused on developing active catalysts that mimic the function of the Ni and Fe centers in CODH to promote the electrochemical reduction of CO₂ [10]. Early studies have focused on low-valent rare metal catalysts (e.g., Re [11,12], Ru [13,14], Ir [15], Rh [16,17]) and have been more recently extended to earth-abundant transition metal catalysts (e.g., Mn [18–22], Fe [8,23–25], Ni [26,27], Co [28–33]). Among those developments, the cobalt complexes, coordinated with ligands such as porphyrin, cyclam, bipyridyl-N-heterocyclic carbene, polypyridines, and aminopyridines, have exhib-

ited promising results in CO₂ reduction, owing to their abundant redox performance and the configurational flexibility provided by these ligands [4,6,34].

Cobalt–porphyrin catalysts have been identified as effective catalysts [28,35–37]. In aqueous buffered solutions, catalytic reduction of CO₂ with CoTCPP (TCPP = meso-tetracarboxyphenylporphine) leads to the formation of formic acid [36]. Catalytic activity has also been observed with other cobalt–porphyrin catalysts, but the products were not identified [28,35,37]. Several other tetraaza-macrocycles related to cobalt cyclams have shown promise as CO₂ reduction catalyst [4,6]. Gangi et al. reported that a cobalt complex with the macrocycle 5,7,7,12,14,14-hexamethyl-1,4,8,11-tetraazacyclotetradeca-4,11-diene exhibits a strong positive shift in the Co^{II/I} reduction potential in the presence of CO₂ and has an equilibrium constant of 7×10^4 for CO₂ binding [38]. Cobalt aminopyridyl macrocycle catalysts have also exhibited an advantageous performance as a pivotal constituent of cobalt complexes [4,6]. The cobalt complex [Co^{III}N₄H(Br)₂]⁺ (N₄H = 2,12-dimethyl-3,7,11,17-tetraazabicyclo-[11.3.1]-heptadeca-1(7),2,11,13,15-pentaene), which is known to be competent for electrocatalytic H₂ evolution, with a redox active pyridyldiimine moiety could electro-catalyze CO₂ to CO in CO₂-saturated solutions of MeCN with 10 M H₂O (F_{CO} = 45% ± 6.4) [29]. Jurss et al. showed a series of cobalt catalysts bearing redox-active ligands, based on bipyridyl-N-heterocyclic carbene donors, exhibiting an excellent efficiency for reducing CO₂ to CO [30]. Marinescu et al. synthesized several macrocyclic catalysts based on azacalix[4](2,6)pyridines. The results indicate that the presence of the pendant NH moiety of the secondary groups leads to a positive shift in the reduction potential of the Co^{I/0} couple, and therefore decreases the overpotential for CO₂ reduction [31,32,39,40]. Cobalt–polypyridine catalysts are also highly active catalysts [33,41]. Quarter-pyridine [Co(qpy)(H₂O)₂]²⁺ (qpy = 2,2':6',2'':6'',2''':6'''-quaterpyridine) complex proved to be an active catalyst for CO₂ to CO (F_{CO} = 90%) reduction at low overpotential of 140 mV in acetonitrile solution with the presence of 3 M phenol [33].

Though different ligands are involved, one of the key steps in a catalytic CO₂ reduction is the coordination of CO₂ molecules to the active site by the reduction catalyst. Herein, we selected capsule-like cobalt(II)–polypyridine diamine complexes [Co(L¹)](BF₄)₂ (**1**; L¹ = N,N,N',N'-tetrakis((6-methylpyridin-2-yl)methyl)ethane-1,2-diamine) and [Co(L²)](CH₃CN)](BF₄)₂ (**2**; L² = N-benzyl-N,N',N'-tris((6-methylpyridin-2-yl)methyl)ethane-1,2-diamine) (Scheme 1) as target catalysts. Under catalytic conditions, complexes **1** and **2** demonstrated the electrocatalytic reduction of CO₂ to CO in the presence or absence of CH₃OH as a proton source. The results of the cyclic voltammograms (CVs) revealed that the doubly reduced intermediates [Co⁰(L¹)]⁰ and [Co⁰(L²)]⁰ were the catalytic active state. Furthermore, we carefully demonstrated the direct reaction between [Co⁰(L¹)]⁰ or [Co⁰(L²)]⁰ and CO₂ through FTIR, HRMS, and DFT studies. The results demonstrate that the metalcarboxylate intermediate [Co^{II}(L)–CO₂²⁻]⁰ was successfully detected. Additionally, it is observed that methanol as proton source could accelerate the rate of carbon–oxygen bond breaking of the metalcarboxylate intermediate. Furthermore, it is revealed that the catalytic cycle is mediated by the cobalt core and involves two crucial intermediates, namely [Co^{II}(L¹)–CO₂²⁻]⁰ and [Co^I(L¹)–CO]⁺.



Scheme 1. The structures of the target cobalt complexes **1** and **2**.

2. Results and Discussion

2.1. Synthesis, Characterization, and X-ray Structures

The mononuclear cobalt complex $[\text{Co}(\text{L}^1)](\text{BF}_4)_2$ (**1**) was conveniently prepared by reacting $\text{Co}(\text{BF}_4)_2 \cdot 6\text{H}_2\text{O}$ with L^1 in acetonitrile at room temperature under ambient air conditions (see the experiment section). A mauve crystalline solid of complex **1** was obtained with a yield of 85%. Complex **2** was synthesized and purified using the same method, yielding 82%. The high-resolution mass spectra (HRMS) and elemental analysis data of complexes **1** and **2** are consistent with the proposed composition of $[\text{Co}(\text{L}^1)](\text{BF}_4)_2$ and $[\text{Co}(\text{L}^2)(\text{CH}_3\text{CN})](\text{BF}_4)_2$.

The molecular structures of complexes **1** and **2** were determined by single crystal X-ray crystallography (Figure 1). Complex **1** adopts a distorted octahedral geometry. The Co–N bond distances for two axial pyridyl–nitrogen atoms (Co–N5 (N6) = 2.292 (2.326) Å) are significantly longer than that of the other four nitrogen atoms on the equatorial plane (Co–N1 (N2, N3, N4) = 2.193 (2.164, 2.147, 2.186) Å). Two pyridine rings on the equatorial plane in complex **1** form an angle of extrusion of 34° . By replacing one of the 6-methylpyridinyls in **1** with phenyl, complex **2** features one CH_3CN solvent molecule coordinated in the equatorial site. Complex **2** shows a normal octahedral geometry, however, its bond lengths and angles are very similar to those in complex **1**. Detailed crystallographic data and processing parameters are collected in Tables S1 and S2.

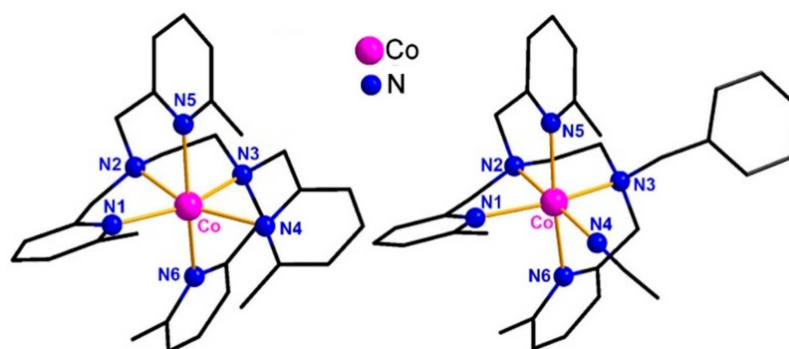


Figure 1. Molecular structures of complexes **1** and **2**. Counter ions and hydrogen atoms are omitted for clarity.

2.2. Electrochemistry

Cyclic voltammograms (CVs) of complex **1** under Ar in CH_3CN solution feature two reversible couples at -1.66 and -1.89 V (all potentials given in this paper are versus ferrocene ($\text{Fc}^{+/0}$)) (Figure 2, black line). The free ligand L^1 is a silent electrochemical in the potential range (Figure S1). Additionally, the absence of any redox processes for a Cu analogue $[\text{Cu}(\text{L}^1)](\text{BF}_4)_2$ between the potentials of -1.66 to -1.89 V (Figure S2) confirms that the ligand is not responsible for the redox events observed for complex **1**. The results reveal that the two couples can be assigned to $\text{Co}^{\text{II/I}}$ and $\text{Co}^{\text{I/0}}$, respectively. The CV of complex **2** (Figure S3) shows almost the same redox couples as **1**. Under the same test conditions, linear sweep voltammograms (LSV) of both complexes **1** and **2** also performed the same redox couples as the reduction waves in the CVs (Figures S4 and S5). Both the first and second couples of complexes **1** and **2** show a good linear relationship between the peak current and squared root of the scan rate, but a difference in slope, indicating that complexes **1** and **2** are functioning in a diffusion-controlled regime and are molecular in nature (Figures S6 and S7). As the scan rate decreases, the ratio of the second peak current to the first increases. Differential pulse voltammograms (DPVs) of complexes **1** and **2** both exhibit two reduction peaks around -1.64 and -1.85 V (Figure S8), which are in accordance with the reduction waves in CVs. Differences in amplitude between $\text{Co}^{\text{II/I}}$ and $\text{Co}^{\text{I/0}}$ for both complexes **1** and **2** in the CVs and DPVs may have resulted from minor changes in configuration following the first electron transfer process of $\text{Co}^{\text{II/I}}$.

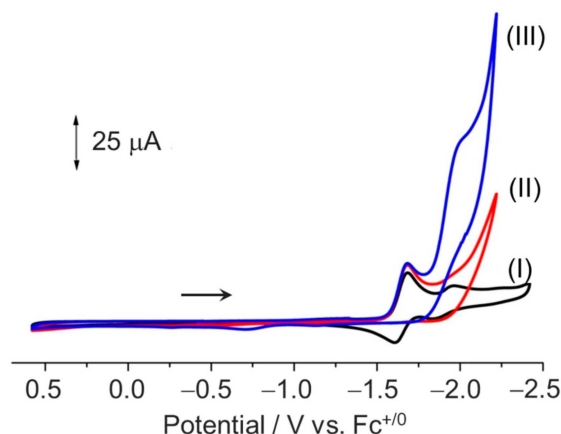


Figure 2. Cyclic voltammograms of complex **1** in CH_3CN with 0.1 M nBu_4NPF_6 as the supporting electrolyte (I) under Ar; under CO_2 (II) in the absence of and (III) in the presence of 4 M methanol. The arrow in the CV diagram represents the initial scan direction.

Under CO_2 , complex **1** exhibits a slight current enhancement around -1.85 V, which is near the potential for $\text{Co}^{\text{I}/0}$ couple (Figure 2, red line; Figure S4). A controlled potential electrolysis (CPE) experiment of complex **1** was performed at -1.9 V under CO_2 . Thereafter, an analysis of the gas mixture, in the headspace of the working compartment of the electrolysis cell, by gas chromatography (GC) identified CO as the exclusive gaseous product under the test condition (Figure S9). The catalytic peak current (i_{cat}) varies linearly with the concentration of complex **1**, consistent with a mechanism for catalytic CO_2 reduction that is a first-order reaction in complex **1** (Figure S10). Under CO_2 in the presence of 4 M methanol, the current exhibits a 4.8-fold increase under CO_2 conditions in the absence of methanol at -2.1 V (Figure 2 and Figure S11). As documented in the literature, this phenomenon is ascribed to methanol's role as a proton source, leading to the modification of the catalytic reaction pathway, thereby enhancing the rate of carbon–oxygen bond cleavage of the metalcarboxylate intermediate [4,6,41] (See details in the “The Analysis of Process and Intermediates”). In addition, the catalytic peak current has linear dependence on methanol concentration, ranging from 0.15 to 0.98 M, and reaching saturation at around 4 M (Figure S11). Changing the sequence of bubbling with CO_2 and adding methanol results in negligible differences in CVs. In contrast, the addition of methanol results in a 260 mV negative shift of the second couple under Ar (Figure 2 and Figure S12). This observation indicates that CO_2 is much more competitive than methanol to coordinate with the reduced catalyst. Under the same test conditions, complex **2** performs an almost identical phenomenon with complex **1** (Figures S5 and S13–S17).

2.3. The Catalytic Rate and Stability of Cobalt Complexes

Under slower scan rates (0.01 to 0.075 V s^{-1}) with 4 M MeOH, the CVs of complexes **1** and **2** show a steady “S-shaped” wave (Figures S18 and S19). Higher scan rates lead to the combination of catalytic current plateaus, followed by subsequent increases in current. Using methods described by Savéant [42,43], the turnover frequency (TOF) values for complexes **1** and **2** are estimated to be 2.03 and 1.57 s^{-1} , respectively, under the scan rate at 0.05 V s^{-1} , with an overpotential around 550 mV (Figures S18 and S19).

A CPE experiment of complex **1** at -2.1 V under CO_2 shows the CO concentration increases as time goes on (Figure S20 inset). The gas chromatography (GC) analysis confirms that the measured CO production matches well with the theoretical yield (Figure S20), indicating that the faradaic efficiency is close to 100%. However, decomposition of the catalyst under highly reductive conditions results in the CO production deviating from its theoretical yield after 3 h (Figures S20–S22). An average turn-over number (TON) of 9.5 was achieved by complex **1**. Between the changes in complex **1** and **2**, an insignificant difference in catalytic activity and stability was found (Figures S23–S25 and Table S4).

In the presence of methanol under CO₂ atmosphere, an 80 min CPE experiment of complex **1** performed at −2.1 V. GC analysis shows that CO and H₂ were the main products. The faradaic efficiency of CO is approximately 30% within 40 min and shows a gradually decreasing trend, dropping to 7% at 80 min. The faradaic efficiency of H₂ gradually increased, reaching 85% at 80 min (Figure S26). Additionally, obvious deposits were observed on the surface of glass carbon electrode after electrolysis for 80 min (Figure S27). This phenomenon is commonly observed in published papers for molecular catalysts, where the predominant component of deposition is a zero-valent metal, accompanied by a minor presence of metal oxide [31,44–46]. The chemical state of the deposits on the surface of glass carbon electrode were investigated by XPS. As shown in Figure S28, the peak with binding energies at 778.5 eV are associated with the zero-valent cobalt, and the peak of 779.5 and 781.1 eV binding energies stem from the cobalt in the oxidation state. The area of the three peaks indicates that the zero-valent cobalt is the predominant component in our experimental deposition. The obtained results align with the findings reported in published papers on cobalt molecular catalysts [31]. The deposited glass carbon electrode, acting as the working electrode, was used at −2.1 V in the presence of methanol under CO₂ atmosphere without complex **1** or **2**. Thereafter, GC analysis shows that H₂ was the sole product. The results reveal that deposits are incapable of catalyzing the reduction of CO₂; their catalytic activity is limited to the reduction of protons for hydrogen gas production. The actual catalyst responsible for the conversion of CO₂ into CO is complexes **1** or **2** in CH₃CN solution.

2.4. The Process and Intermediates Analysis

The initial step in the reduction of CO₂ molecules involves its binding. As shown in Figure 2, in the presence of CO₂, [Co⁰(L¹)]⁰ is sensitive to CO₂ such that slightly more negative scanning following Co^{II/I} would result in the irreversibility of the Co^{I/0} and Co^{II/I} couple (Figure S29). In the DPV test of complex **1** under CO₂, the first peak shows no difference with that under Ar, but the second peak expands to a plateau (Figure S30), indicating that CO₂ binding and subsequent reduction coincide with the Co^{I/0} couple. In the presence of 4 M methanol, the plateau splits into two stronger peaks. The more positive one could be ascribed to the formation of a CO₂ adduct [Co^{II}(L¹)–COOH[−]]⁺. The other corresponds to the following reduction. Additionally, the reduction of complex **1** is restricted to the [Co^I(L¹)]⁺ state by mixing complex **1** with 1 equiv of bis-pentamethylcyclopentadienyl-cobalt(II) (Cp*₂Co, the oxidation potential of Cp*₂Co is −1.82 V vs. Fc^{+ /0} in CH₃CN). Then, the addition of dry CO₂ brings no new absorption band attributed to carbonyl. Herein, it can be concluded that [Co⁰(L¹)]⁰ is the active state for CO₂ rather than [Co^I(L¹)]⁺, and two-electron reduction are necessary to activate complex **1**.

[Co⁰(L¹)]⁰ as a dark blue solution in a mixture of CH₃CN/THF (1:1) can be easily prepared by chemical reduction of complex **1** with 2 equiv of NaHg. When the solution is bubbled with dry CO₂ gas, the color changes back to mauve in 30 s (Figure S31). As we know, the blue color is attributed to the electron transfer between d orbitals of cobalt. The significant change in color indicates two electrons are transferring from cobalt to CO₂. Then, we monitor the process of CO₂ coordinating with [Co⁰(L¹)]⁰ by in situ FTIR (Figure 3 and Figure S32). In the range of 1200 to 2500 cm^{−1}, [Co⁰(L¹)]⁰ shows a slight IR absorption. When dry CO₂ is added, a weak broad absorption appears at 1669 cm^{−1}, indicating that CO₂ coordinates with [Co⁰(L¹)]⁰ to form the intermediate [Co^{II}(L¹)–CO₂^{2−}] (Figure 3). The frequency is close to that reported for Co(salen)CO₂Na (1680 cm^{−1}) [47]. Then, upon addition of methanol, three new bands appeared at 1634, 1481, and 1390 cm^{−1} (Figure 3 and Figure S33). The assignment was confirmed by isotope labelling experiment. When dry ¹³CO₂ is introduced, followed by the addition of methanol, these new bands shift toward lower wavenumbers by 30 to 60 cm^{−1} (Figure 3). We conclude that methanol disrupts the balance of electron distribution on the two oxygen atoms of CO₂, resulting ultimately in coordinated transformation into the metalcarboxylate intermediate (Figure 3). Therefore,

in this catalysis system, methanol could lead to the CO₂ binding equilibrium moving toward the forward reaction.

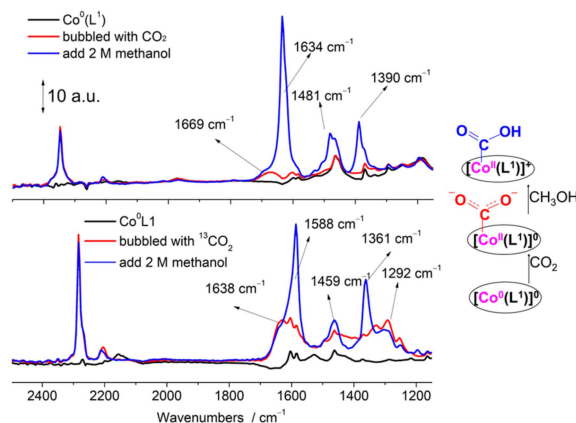


Figure 3. IR spectrum of freshly prepared $[\text{Co}^0(\text{L}^1)]^0$ (black line), which is bubbled with dry CO₂ (above) and ¹³CO₂ (down) (red line), then 2 M methanol is added (blue line). These lines were recorded by in situ FTIR during the reaction process. The tests are performed in a CH₃CN/THF (1:1) mixture under Ar or CO₂ with 10.0 mM $[\text{Co}^0(\text{L}^1)]^0$.

The fresh reaction solution is then analyzed by high resolution mass spectrometry (HRMS) [48]. The isotope distribution pattern at $m/z^- = 584.2305, 585.2333$ and 586.2363 fit well with the calculated isotope distribution pattern of the mass fragment $[\text{Co}^{\text{II}}(\text{L}^1)\text{-COOH}]^+$. The results reveal that we successfully detected the protonated product of $[\text{Co}^{\text{II}}(\text{L}^1)\text{-CO}_2^{2-}]^0$ (Figure 4 and Figure S34). In the same way, the protonated product of $[\text{Co}^{\text{II}}(\text{L}^2)\text{-CO}_2^{2-}]^0$ (Figures S35 and S36), prepared from the analogue complex **2**, was also detected by HRMS and it was found that the acetonitrile ligand had dissociated from cobalt. These results provide clear evidence for the incorporation of CO₂ into the $[\text{Co}^0(\text{L}^1)]^0$ intermediate.

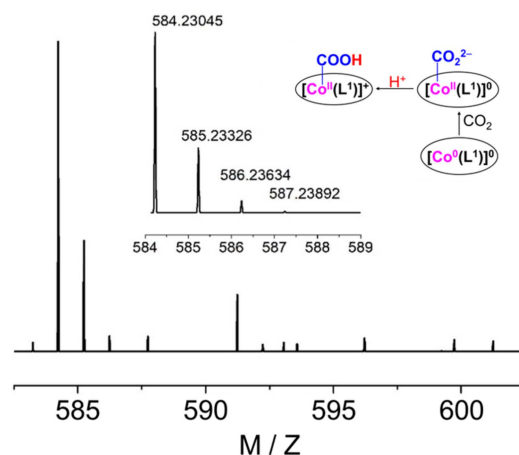


Figure 4. The observed and calculated (inset) HRMS of the protonated product of $[\text{Co}^{\text{II}}(\text{L}^1)\text{-CO}_2^{2-}]^0$ generated from CO₂ coordinating to $[\text{Co}^0(\text{L}^1)]^0$.

As referred to in the DPV test of complex **1** under CO₂, CO₂ binding and the following reduction coincide with the Co^{I/0} couple (Figure S30). To investigate the subsequent reduction of the CO₂-coordinated cobalt metalcarboxylate, in situ infrared spectroelectrochemistry (IR-SEC) experiments are performed at -1.85 V. The differential IR-SEC spectrum of **1** reveals a decrease in CO₂ intensity around 2340 cm⁻¹ and the emergence of a band at 1917 cm⁻¹ (Figure 5). Complex **1** itself does not possess IR absorption modes with sufficient intensity that can be distinguished within the range of

1500 to 2500 cm^{-1} , under varied electrolysis potential from -1.0 to -2.4 V, and in the absence of CO_2 . The absorption peak observed at 1917 cm^{-1} can be ascribed to the two-electron reduction species $[\text{Co}^{\text{I}}(\text{L}^1)\text{-CO}]^+$ [26,49], which is obtained from through further reduction of $[\text{Co}^{\text{II}}(\text{L}^1)\text{-CO}_2^{2-}]^0$. Fujita and colleagues have reported that $[\text{Co}^{\text{I}}(\text{macrocycle})\text{-CO}]^+$ (macrocycle = 5,7,7,12,14,14-hexamethyl-1,4,8,11-tetraazacyclotetradeca-4,11-diene) exhibits an absorption peak at 1916 cm^{-1} [49,50]. Upon reduction of complex **1** with 1 equiv of Cp^*_2Co under CO , a weak IR absorption band resembling $[\text{Co}^{\text{I}}(\text{macrocycle})\text{-CO}]^+$ was observed at 1917 cm^{-1} (Figure S37). In the presence of 1 M methanol under the same experimental condition, two strong peaks at 1916 and 1664 cm^{-1} were ascribed to $[\text{Co}^{\text{I}}(\text{L}^1)\text{-CO}]^+$ and the combination absorption of $[\text{Co}^{\text{II}}(\text{L}^1)\text{-COOH}^-]^+$, respectively (Figure S38). The differential IR-SEC spectrum of complex **2** was also recorded at -1.85 V. Similar to complex **1**, the peak of the reduction species $[\text{Co}^{\text{I}}(\text{L}^2)\text{-CO}]^+$ was also observed at 1917 cm^{-1} . The findings suggest that complex **2** undergoes the same catalytic mechanism as complex **1**. (Figure S39). Consequently, there will be further reductions of CO_2 -coordinated cobalt intermediates to generate CO .

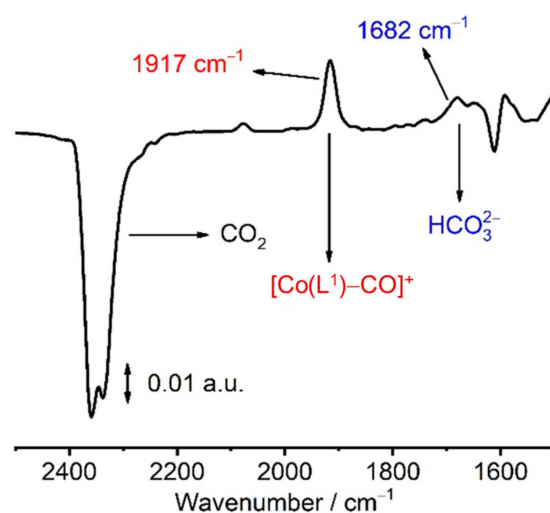


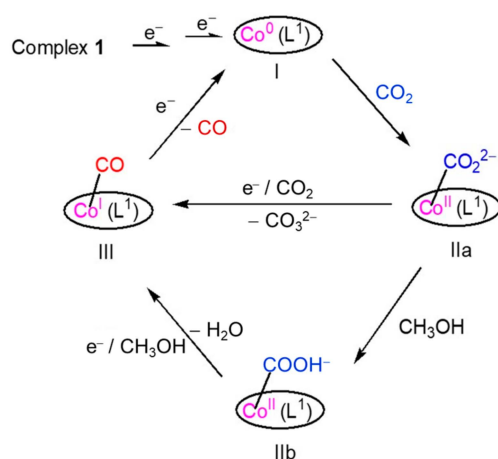
Figure 5. Differential IR-SEC spectrum of complex **1** (10.0 mM) recorded after electrolysis at -1.85 V (vs. $\text{Fc}^{+/0}$) for 10 s in CO_2 saturated CH_3CN solution.

2.5. Density Functional Theory (DFT) Calculation and Mechanistic Consideration

To get a better understanding of the electronic distribution on the reduced catalyst $[\text{Co}^0(\text{L}^1)]^0$, we employed DFT calculations using Gaussian 09, Revision D.01. Firstly, the geometry-optimized initial structure of $[\text{Co}^{\text{I}}(\text{L}^1)]^+$ shows that both pyridine groups in the axial direction dissociate from cobalt (Figure S40a). The dissociation is consistent with the longer C–N distance in the axial direction. The dissociation results in a minor change in configuration, which leads to the difference in current amplitude for the two reduction peaks in complex **1** (Figure 2). As proven above, CO_2 coordination is coupled with the second reduction. After which, the CO_2 molecule is joined to the optimized structure $[\text{Co}^{\text{I}}(\text{L}^1)]^+$ at the axial open site. Meanwhile, the second electron is added. The geometry-optimized electronic structure of $[\text{Co}^{\text{II}}(\text{L}^1)\text{-CO}_2^{2-}]^0$ shows the electron density distribution in the frontiers (Figure S40b). The optimized structure provides evidence supporting the hypothesis that CO_2 can undergo an attack by the d_{z^2} orbital of the doubly reduced cobalt from the axial direction. The formation of a σ bond between the d_{z^2} orbital and the carbon atom of CO_2 (HOMO) is observed, and this interaction with CO_2 can be further stabilized through π interactions between the metal's d_{xz} or d_{yz} orbitals and p orbitals on the oxygen atoms of CO_2 (HOMO–5, Figure S41). The results of the Kubiak and Fujita groups are also similar in that the stabilizing interaction is with oxygen atoms of CO_2 rather than the carbon atom [51]. This tridentate interaction makes the coordination of CO_2 to $[\text{Co}^0(\text{L}^1)]^0$ irreversible. Furthermore, the attack on the oxygen atom by Brønsted acid

becomes more favorable. The optimized $[\text{Co}^{\text{II}}(\text{L}^1)\text{-CO}_2^{2-}]^0$ shows that one dissociated pyridine in $[\text{Co}^{\text{I}}(\text{L}^1)]^+$ state stabilizes the CO_2 adduct from the axial direction (Figure S38). Compared with **1**, **2** features one labile CH_3CN ligand. The reductive dissociation of the labile ligand acetonitrile from the polypyridine–cobalt complexes at the $[\text{Co}^{\text{I}}]$ state has been previously verified by other groups. By replacing acetonitrile with CO_2 , while two electrons are also added, the geometry-optimized electronic structure of $[\text{Co}^{\text{II}}(\text{L}^2)\text{-CO}_2^{2-}]^0$ gives rise to almost the same electronic structure as $[\text{Co}^{\text{II}}(\text{L}^1)\text{-CO}_2^{2-}]^0$ (Figures S42 and S43). Thus, we conclude complex **2** to be a simpler model for CO_2 reduction.

Taking complex **1** as an example, Scheme 2 summarizes a proposed mechanism for the catalytic reduction of CO_2 to CO by complexes **1** and **2**. Initially, a two-electron reduction is necessary to generate the active complex $[\text{Co}^0(\text{L}^1)]^0$ (**I**). As $[\text{Co}^0(\text{L}^1)]^0$ is so sensitive, CO_2 is coordinated to generate $[\text{Co}^{\text{II}}(\text{L}^1)\text{-CO}_2^{2-}]^0$ (**IIa**). Subsequently, the carbon–oxygen bond cleavage have two paths: (1) another one-electron reduction that leads to O^{2-} transferring to another CO_2 molecule, resulting in the intermediate of $[\text{Co}^{\text{I}}(\text{L}^1)\text{-CO}]^+$ (**III**) and coproduct CO_3^{2-} ; or (2) the intermediate of $[\text{Co}^{\text{II}}(\text{L}^1)\text{-COOH}]^+$ (**IIb**) is formed first in the presence of CH_3OH as a proton source, and it then receives an electron and undergoes reduction, leading to the cleavage of the carbon–oxygen bond and generating the intermediate $[\text{Co}^{\text{I}}(\text{L}^1)\text{-CO}]^+$ (**III**) and coproduct H_2O . Finally, one more electron is required to release CO and regenerate $[\text{Co}^0(\text{L}^1)]^0$. The involvement of intermediates $[\text{Co}^{\text{II}}(\text{L}^1)\text{-CO}_2^{2-}]^0$ (**IIa**) and $[\text{Co}^{\text{I}}(\text{L}^1)\text{-CO}]^+$ (**III**) indicates that the cobalt core mediates this catalytic process.



Scheme 2. A proposed mechanism for electroreduction of CO_2 to CO catalyzed by complex **1**.

3. Materials and Methods

3.1. Materials and Instruments

All manipulations for the preparation and handling of the organometallic complexes were carried out under air. All the solvents were used as received. Other commercially available chemicals, such as $\text{Co}(\text{BF}_4)_2 \cdot 6\text{H}_2\text{O}$, 1,2-ethanediamine, 6-methylpicolinaldehyde, N-benzylethane-1,2-diamine, were purchased from local suppliers and used as received. Water was deionized with the Millipore Milli-Q UF Plus system. Glass carbon discs (3 mm), AgCl/Ag electrodes and platinum wire were purchased from CHI for electrochemical studies. Arrows are employed in the CV diagram to denote the initial scanning direction.

The NMR spectrum was acquired by employing the Varian INOVA 600 NMR spectrometer, an instrument manufactured by the renowned American company Varian. Mass spectra were recorded with HP 1100 HPL/ESI-DAD-MS and Waters/Micromass LC/Q-TOF-MS instruments. Elemental analyses were performed with a Thermoquest-Flash EA 1112 elemental analyzer. FTIR in situ was monitored by React IR 15 instrument equipped with a MCT detector and a Dsub AgXSiComp in situ probe.

3.2. Synthesis

Synthesis of ligands L^1 and L^2 . L^1 and L^2 were prepared according to the procedures in the literature [52,53].

L^1 : $^1\text{H NMR}$ (CDCl_3 , 400 MHz), δ 7.45 (d, 4H), 7.32 (m, 4H), 6.95 (d, 4H), 3.75 (s, 8H), 2.76 (s, 4H), 2.49 (s, 12H).

L^2 : $^1\text{H NMR}$ (CDCl_3 , 400 MHz), δ 7.45 (m, 4H), 7.26 (m, 6H), 6.70 (m, 4H), 3.75 (s, 6H), 3.59 (s, 2H), 2.76 (d, 4H), 2.50 (s, 9H).

Preparation of complexes **1** and **2**. Compound $\text{Co}(\text{BF}_4)_2 \cdot 6\text{H}_2\text{O}$ (1.1 equiv) and L^1 (1.0 equiv) or L^2 (1.0 equiv) were added to the CH_3CN solution (5 mL). The mixture was stirred at room temperature for 12 h. The mauve solution was then transferred to tubes, which were placed in the flask containing ether, and needle-shaped crystals were obtained.

Complex **1**: elemental analysis calcd (%) for $\text{C}_{30}\text{H}_{36}\text{B}_2\text{CoF}_8\text{N}_6$ (%): C, 50.53; H, 5.08; N, 11.77; found: 50.52; H, 5.09; N, 11.78; HRMS: $m/z = 269.6641 \{[\text{M}-2(\text{BF}_4)^-]/2\}^+$, 574.3025 $[\text{M}-2(\text{BF}_4)^- + \text{Cl}^-]^+$.

Complex **2**: elemental analysis calcd (%) for $\text{C}_{32}\text{H}_{38}\text{B}_2\text{CoF}_8\text{N}_6$ (%): C, 51.98; H, 5.19; N, 11.38 found: C, 52.00; H, 5.19; N, 11.39; HRMS: $m/z = 262.1598 \{[\text{M}-2(\text{BF}_4)^- - \text{CH}_3\text{CN}]/2\}^+$, 559.3027 $[\text{M}-2(\text{BF}_4)^- - \text{CH}_3\text{CN} + \text{Cl}^-]^+$.

In situ preparation of $[\text{Co}^0(\text{L}^1)]^0$. Complex **1** was mixed with 2.0 equiv of $\text{Na}(\text{Hg})$ in a highly pure THF and CH_3CN (1:1) mixture under Ar. The sample was stirred under Ar overnight. A dark blue solvent appeared after stirring stopped. The freshly prepared $[\text{Co}^0(\text{L}^1)]^0$ was used in the next step without further handling.

In situ preparation of $[\text{Co}^{\text{II}}(\text{L}^1)-\text{CO}_2^{2-}]^0$. The reaction was monitored by a React IR 15 instrument equipped with a MCT detector and a Dsub AgXSiComp in situ probe. The experiment was performed at room temperature. $[\text{Co}^{\text{II}}(\text{L}^1)-\text{CO}_2^{2-}]^0$ was prepared by bubbling dry CO_2 into the solution of complex $[\text{Co}^0(\text{L}^1)]^0$. In about 30 s, the dark blue color changed back to pink. After which, 2 M of CH_3OH was added into the solvent. The fresh reaction solution was tested directly by a mass spectrum.

In situ preparation of $[\text{Co}^{\text{II}}(\text{L}^1)-\text{CO}]^{2+}(\text{BF}_4)_2$ and $[\text{Co}^{\text{I}}(\text{L}^1)-\text{CO}]^+(\text{BF}_4)$. The reaction was monitored by a React IR 15 instrument equipped with a MCT detector and a Dsub AgXSiComp in situ probe. The experiment was performed at room temperature. $[\text{Co}^{\text{II}}(\text{L}^1)-\text{CO}]^{2+}(\text{BF}_4)_2$ was prepared by bubbling CO into the solution of complex $[\text{Co}(\text{L}^1)](\text{BF}_4)_2(\mathbf{1})$ in acetonitrile. In about 3 min, the absorption attributed to $[\text{Co}^{\text{II}}(\text{L}^1)-\text{CO}]^{2+}(\text{BF}_4)_2$ reached the highest intensity. $[\text{Co}(\text{L}^1)-\text{CO}]^+(\text{BF}_4)^-$ was prepared by the addition of 1 equiv Cp^*Co (Bis-pentamethylcyclopentadienyl-cobalt(II)) into the solution of complex $[\text{Co}(\text{L}^1)](\text{BF}_4)_2$ in acetonitrile under CO atmosphere. In about 3 min, the absorption attributed to $[\text{Co}(\text{L}^1)-\text{CO}]^+(\text{BF}_4)^-$ reached the highest intensity.

3.3. IR-SEC Test Details

The spectroelectrochemical experiments were conducted using an IFS 66v/S FTIR spectrometer (Bruker) equipped with an MCT-A detector. Electrode potential was controlled using a model CHI potentiostat. The SEC experiments were performed in a homemade three-neck cell with a glassy carbon electrode serving as the working electrode, while a platinum foil acted as the counter electrode, and Ag/AgCl (3 M KCl) as the reference electrode. IR-SEC spectra were collected in a single beam mode at either 2 cm^{-1} or 4 cm^{-1} , and differential absorption spectra were presented relative to the reference spectrum and were recorded immediately prior to applying the potential.

3.4. Computational Methods

All DFT computations were calculated at the B3LYP (the Becke three-parameter Lee–Yang–Parr hybrid functional) level using the 6-31G(d) basis set for all atoms via the Gaussian 09 program package [54,55]. All structures were fully optimized and confirmed as minima by analytical vibrational frequency calculations with B3LYP/6-31G(d). The solvent acetonitrile was modeled as a dielectric continuum using a polarizable continuum model (PCM).

The basis sets and solvent model were adopted to predict CO coordinates and the results were in good agreement with X-ray crystal structure [56]. All calculated structures were visualized by Gauss View 5.0.9.

4. Conclusions

In conclusion, this paper provides a comprehensive investigation into the electrocatalytic reduction of CO₂ to CO mediated by the capsule-like cobalt(II)–polypyridine diamine complexes **1** and **2**. The catalytically active state is represented by [Co⁰(L¹)]⁰ or [Co⁰(L²)]⁰. The catalytic cycle involves crucial intermediates, namely [Co^{II}(L)–CO₂²⁻]⁰ and [Co^I(L)–CO]⁺, with the cobalt core playing a central role. These findings provide comprehensive mechanistic insights into a class of catalysts enabling the sustained electrocatalytic reduction of CO₂ to CO, emphasizing the crucial role of prior reductions on cobalt alone. These discoveries have guided us in synthesizing a series of cobalt-based complexes with secondary coordination spheres (such as hydroxyl, carboxyl, and amino groups) to facilitate the cleavage of carbon–oxygen bonds in intermediates, thereby enhancing the electrocatalytic performance for the CO₂ reduction exhibited by these cobalt-based complexes.

Supplementary Materials: The following supporting information can be downloaded at: <https://www.mdpi.com/article/10.3390/molecules29081694/s1>.

Author Contributions: Y.Y.: conceptualization, methodology, writing—review and editing, supervision, project administration, funding acquisition, resources, validation. F.X.: methodology, validation, investigation, writing—original draft. J.C.: methodology, validation, investigation, data curation. S.Q., N.Q., M.L. and Z.P.: review and editing. J.Y. and G.L.: methodology, validation, investigation, funding acquisition, writing—review and editing, supervision, project administration. All authors have read and agreed to the published version of the manuscript.

Funding: This work was supported by Youth Innovative Talents Projects in Colleges and Universities in Guangdong Province (2022KQNCX082); Guangdong Basic and Applied Basic Research Foundation (2022A1515110778, 2023A1515140150); National Natural Science Foundation of China (22101186, 51162026), Natural Science Foundation of Top Talent of SZTU (GDRC202114); Key Projects of the Guangdong Education Department (2021ZDJS081, 2022ZDJS054).

Institutional Review Board Statement: Not applicable.

Informed Consent Statement: Not applicable.

Data Availability Statement: Data are contained within the article and Supplementary Materials.

Conflicts of Interest: The authors declare no conflicts of interest.

References

1. Davis, S.J.; Caldeira, K.; Matthews, H.D. Future CO₂ Emissions and Climate Change from Existing Energy Infrastructure. *Science* **2010**, *329*, 1330–1333. [[CrossRef](#)] [[PubMed](#)]
2. Chen, C.; Khosrowabadi Kotyk, J.F.; Sheehan, S.W. Progress toward Commercial Application of Electrochemical Carbon Dioxide Reduction. *Chem* **2018**, *4*, 2571–2586. [[CrossRef](#)]
3. Benson, E.E.; Kubiak, C.P.; Sathrum, A.J.; Smieja, J.M. Electrocatalytic and Homogeneous Approaches to conversion of CO₂ to Liquid Fuels. *Chem. Soc. Rev.* **2009**, *38*, 89–99. [[CrossRef](#)] [[PubMed](#)]
4. Boutin, E.; Merakeb, L.; Ma, B.; Boudy, B.; Wang, M.; Bonin, J.; Anxolabéhère-Mallart, E.; Robert, M. Molecular Catalysis of CO₂ Reduction: Recent Advances and Perspectives in Electrochemical and Light-driven Processes with Selected Fe, Ni and Co Aza macrocyclic and Polypyridine Complexes. *Chem. Soc. Rev.* **2020**, *49*, 5772–5809. [[CrossRef](#)] [[PubMed](#)]
5. Kinzel, N.W.; Werlé, C.; Leitner, W. Transition Metal Complexes as Catalysts for the Electroconversion of CO₂: An Organometallic Perspective. *Angew. Chem. Int. Ed.* **2021**, *60*, 11628–11686. [[CrossRef](#)] [[PubMed](#)]
6. Droghetti, F.; Amati, A.; Ruggi, A.; Natali, M. Bioinspired Motifs in Proton and CO₂ Reduction with 3d-metal Polypyridine Complexes. *Chem. Commun.* **2024**, *60*, 658–673. [[CrossRef](#)] [[PubMed](#)]
7. Costentin, C.; Drouet, S.; Robert, M.; Savéant, J.-M. Turnover Numbers, Turnover Frequencies, and Overpotential in Molecular Catalysis of Electrochemical Reactions. Cyclic Voltammetry and Preparative-Scale Electrolysis. *J. Am. Chem. Soc.* **2012**, *134*, 11235–11242. [[CrossRef](#)] [[PubMed](#)]

8. Azcarate, I.; Costentin, C.; Robert, M.; Savéant, J.-M. Through-Space Charge Interaction Substituent Effects in Molecular Catalysis Leading to the Design of the Most Efficient Catalyst of CO₂-to-CO Electrochemical Conversion. *J. Am. Chem. Soc.* **2016**, *138*, 16639–16644. [[CrossRef](#)]
9. Jeoung, J.-H.; Dobbek, H. Carbon Dioxide Activation at the Ni,Fe-Cluster of Anaerobic Carbon Monoxide Dehydrogenase. *Science* **2007**, *318*, 1461–1464. [[CrossRef](#)]
10. Can, M.; Armstrong, F.A.; Ragsdale, S.W. Structure, Function, and Mechanism of the Nickel Metalloenzymes, CO Dehydrogenase, and Acetyl-CoA Synthase. *Chem. Rev.* **2014**, *114*, 4149–4174. [[CrossRef](#)]
11. Hawecker, J.; Lehn, J.-M.; Ziessel, R. Electrocatalytic Reduction of Carbon Dioxide Mediated by Re(bipy)(CO)₃Cl (bipy = 2,2'-bipyridine). *J. Chem. Soc. Chem. Commun.* **1984**, *6*, 328–330. [[CrossRef](#)]
12. Smieja, J.M.; Sampson, M.D.; Grice, K.A.; Benson, E.E.; Froehlich, J.D.; Kubiak, C.P. Manganese as a Substitute for Rhenium in CO₂ Reduction Catalysts: The Importance of Acids. *Inorg. Chem.* **2013**, *52*, 2484–2491. [[CrossRef](#)] [[PubMed](#)]
13. Machan, C.W.; Sampson, M.D.; Kubiak, C.P. A Molecular Ruthenium Electrocatalyst for the Reduction of Carbon Dioxide to CO and Formate. *J. Am. Chem. Soc.* **2015**, *137*, 8564–8571. [[CrossRef](#)]
14. Johnson, B.A.; Maji, S.; Agarwala, H.; White, T.A.; Mijangos, E.; Ott, S. Activating a Low Overpotential CO₂ Reduction Mechanism by a Strategic Ligand Modification on a Ruthenium Polypyridyl Catalyst. *Angew. Chem. Int. Ed.* **2016**, *55*, 1825–1829. [[CrossRef](#)]
15. Kang, P.; Cheng, C.; Chen, Z.; Schauer, C.K.; Meyer, T.J.; Brookhart, M. Selective Electrocatalytic Reduction of CO₂ to Formate by Water-Stable Iridium Dihydride Pincer Complexes. *J. Am. Chem. Soc.* **2012**, *134*, 5500–5503. [[CrossRef](#)] [[PubMed](#)]
16. Todorova, T.K.; Huan, T.N.; Wang, X.; Agarwala, H.; Fontecave, M. Controlling Hydrogen Evolution during Photoreduction of CO₂ to Formic Acid Using [Rh(R-bpy)(Cp*)Cl]⁺ Catalysts: A Structure–Activity Study. *Inorg. Chem.* **2019**, *58*, 6893–6903. [[CrossRef](#)] [[PubMed](#)]
17. Caix, C.; Chardon-Noblat, S.; Deronzier, A. Electrocatalytic Reduction of CO₂ into Formate with [(η⁵ Me₅C₅)M(L)Cl]⁺ Complexes (L = 2,2'-bipyridine ligands; M Rh(III) and Ir(III)). *J. Electroanal. Chem.* **1997**, *434*, 163–170. [[CrossRef](#)]
18. Bourrez, M.; Molton, F.; Chardon-Noblat, S.; Deronzier, A. [Mn(bipyridyl)(CO)₃Br]: An Abundant Metal Carbonyl Complex as Efficient Electrocatalyst for CO₂ Reduction. *Angew. Chem. Int. Ed.* **2011**, *50*, 9903–9906. [[CrossRef](#)] [[PubMed](#)]
19. Sampson, M.D.; Nguyen, A.D.; Grice, K.A.; Moore, C.E.; Rheingold, A.L.; Kubiak, C.P. Manganese Catalysts with Bulky Bipyridine Ligands for the Electrocatalytic Reduction of Carbon Dioxide: Eliminating Dimerization and Altering Catalysis. *J. Am. Chem. Soc.* **2014**, *136*, 5460–5471. [[CrossRef](#)]
20. Sung, S.; Li, X.; Wolf, L.M.; Meeder, J.R.; Bhuvanesh, N.S.; Grice, K.A.; Panetier, J.A.; Nippe, M. Synergistic Effects of Imidazolium-Functionalization on fac-Mn(CO)₃ Bipyridine Catalyst Platforms for Electrocatalytic Carbon Dioxide Reduction. *J. Am. Chem. Soc.* **2019**, *141*, 6569–6582. [[CrossRef](#)]
21. Yang, Y.; Ertem, M.Z.; Duan, L. An Amide-based Second Coordination Sphere Promotes the Dimer Pathway of Mn-catalyzed CO₂-to-CO Reduction at Low Overpotential. *Chem. Sci.* **2021**, *12*, 4779–4788. [[CrossRef](#)] [[PubMed](#)]
22. He, S.; Qing, Y.; Zhang, P.; Xiong, Y.; Wu, Q.; Zhang, Y.; Chen, L.; Huang, F.; Li, F. Proton Tunneling Distances for Metal Hydrides Formation Manage the Selectivity of Electrochemical CO₂ Reduction Reaction. *Angew. Chem. Int. Ed.* **2023**, *62*, e202216082. [[CrossRef](#)] [[PubMed](#)]
23. Costentin, C.; Drouet, S.; Robert, M.; Savéant, J.-M. A Local Proton Source Enhances CO₂ Electroreduction to CO by a Molecular Fe Catalyst. *Science* **2012**, *338*, 90–94. [[CrossRef](#)] [[PubMed](#)]
24. Costentin, C.; Robert, M.; Savéant, J.-M.; Tatin, A. Efficient and Selective Molecular Catalyst for the CO₂-to-CO Electrochemical Conversion in Water. *Proc. Natl. Acad. Sci. USA* **2015**, *112*, 6882–6886. [[CrossRef](#)] [[PubMed](#)]
25. Nichols, A.W.; Chatterjee, S.; Sabat, M.; Machan, C.W. Electrocatalytic Reduction of CO₂ to Formate by an Iron Schiff Base Complex. *Inorg. Chem.* **2018**, *57*, 2111–2121. [[CrossRef](#)] [[PubMed](#)]
26. Froehlich, J.D.; Kubiak, C.P. The Homogeneous Reduction of CO₂ by [Ni(cyclam)]⁺: Increased Catalytic Rates with the Addition of a CO Scavenger. *J. Am. Chem. Soc.* **2015**, *137*, 3565–3573. [[CrossRef](#)] [[PubMed](#)]
27. Hong, D.; Tsukakoshi, Y.; Kotani, H.; Ishizuka, T.; Kojima, T. Visible-Light-Driven Photocatalytic CO₂ Reduction by a Ni(II) Complex Bearing a Bioinspired Tetradentate Ligand for Selective CO Production. *J. Am. Chem. Soc.* **2017**, *139*, 6538–6541. [[CrossRef](#)]
28. Enoki, O.; Imaoka, T.; Yamamoto, K. Electrochemical Reduction of Carbon Dioxide Catalyzed by Cofacial Dinuclear Metalloporphyrin. *Macromol. Symp.* **2003**, *204*, 151–158. [[CrossRef](#)]
29. Lacy, D.C.; McCrory, C.C.L.; Peters, J.C. Studies of Cobalt-Mediated Electrocatalytic CO₂ Reduction Using a Redox-Active Ligand. *Inorg. Chem.* **2014**, *53*, 4980–4988. [[CrossRef](#)]
30. Su, X.; McCardle, K.M.; Chen, L.; Panetier, J.A.; Jurss, J.W. Robust and Selective Cobalt Catalysts Bearing Redox-Active Bipyridyl-N-heterocyclic Carbene Frameworks for Electrochemical CO₂ Reduction in Aqueous Solutions. *ACS Catal.* **2019**, *9*, 7398–7408. [[CrossRef](#)]
31. Johnson, E.M.; Liu, J.J.; Samuel, A.D.; Haiges, R.; Marinescu, S.C. Switching Catalyst Selectivity via the Introduction of a Pendant Nitrophenyl Group. *Inorg. Chem.* **2022**, *61*, 1316–1326. [[CrossRef](#)] [[PubMed](#)]
32. Chapovetsky, A.; Liu, J.J.; Welborn, M.; Luna, J.M.; Do, T.; Haiges, R.; Miller III, T.F.; Marinescu, S.C. Electronically Modified Cobalt Aminopyridine Complexes Reveal an Orthogonal Axis for Catalytic Optimization for CO₂ Reduction. *Inorg. Chem.* **2020**, *59*, 13709–13718. [[CrossRef](#)] [[PubMed](#)]

33. Cometto, C.; Chen, L.; Lo, P.-K.; Guo, Z.; Lau, K.-C.; Anxolabéhère-Mallart, E.; Fave, C.; Lau, T.-C.; Robert, M. Highly Selective Molecular Catalysts for the CO₂-to-CO Electrochemical Conversion at Very Low Overpotential. Contrasting Fe vs. Co Quaterpyridine Complexes upon Mechanistic Studies. *ACS Catal.* **2018**, *8*, 3411–3417. [[CrossRef](#)]
34. Chen, L.; Chen, G.; Leung, C.-F.; Cometto, C.; Robert, M.; Lau, T.-C. Molecular Quaterpyridine-based Metal Complexes for Small Molecule Activation: Water Splitting and CO₂ Reduction. *Chem. Soc. Rev.* **2020**, *49*, 7271–7283. [[CrossRef](#)] [[PubMed](#)]
35. Hiratsuka, K.; Takahashi, K.; Sasaki, H.; Toshima, S. Electrocatalytic Behavior of Tetrasulfonated Metal Phthalocyanines in the Reduction of Carbon Dioxide. *Chem. Lett.* **2006**, *6*, 1137–1140. [[CrossRef](#)]
36. Takahashi, K.; Hiratsuka, K.; Sasaki, H.; Toshima, S. Electrocatalytic Behavior of Metal Porphyrins in the Reduction of Carbon Dioxide. *Chem. Lett.* **2006**, *8*, 305–308. [[CrossRef](#)]
37. Behar, D.; Dhanasekaran, T.; Neta, P.; Hosten, C.M.; Ejeh, D.; Hambright, P.; Fujita, E. Cobalt Porphyrin Catalyzed Reduction of CO₂. Radiation Chemical, Photochemical, and Electrochemical Studies. *J. Phys. Chem. A* **1998**, *102*, 2870–2877. [[CrossRef](#)]
38. Gangi, D.A.; Durand, R.R. Binding of Carbon Dioxide to Cobalt and Nickel Tetra-aza Macrocycles. *J. Chem. Soc. Chem. Commun.* **1986**, *9*, 697–699. [[CrossRef](#)]
39. Chapovetsky, A.; Do, T.H.; Haiges, R.; Takase, M.K.; Marinescu, S.C. Proton-Assisted Reduction of CO₂ by Cobalt Aminopyridine Macrocycles. *J. Am. Chem. Soc.* **2016**, *138*, 5765–5768. [[CrossRef](#)]
40. Chapovetsky, A.; Welborn, M.; Luna, J.M.; Haiges, R.; Miller, T.F., III; Marinescu, S.C. Pendant Hydrogen-Bond Donors in Cobalt Catalysts Independently Enhance CO₂ Reduction. *ACS Cent. Sci.* **2018**, *4*, 397–404. [[CrossRef](#)]
41. Cometto, C.; Chen, L.; Anxolabéhère-Mallart, E.; Fave, C.; Lau, T.-C.; Robert, M. Molecular Electrochemical Catalysis of the CO₂-to-CO Conversion with a Co Complex: A Cyclic Voltammetry Mechanistic Investigation. *Organometallics* **2019**, *38*, 1280–1285. [[CrossRef](#)]
42. Costentin, C.; Passard, G.; Robert, M.; Savéant, J.-M. Ultraefficient Homogeneous Catalyst for the CO₂-to-CO Electrochemical Conversion. *Proc. Natl. Acad. Sci. USA* **2014**, *111*, 14990–14994. [[CrossRef](#)] [[PubMed](#)]
43. Nichols, E.M.; Derrick, J.S.; Nistanaki, S.K.; Smith, P.T.; Chang, C.J. Positional Effects of Second-sphere Amide Pendants on Electrochemical CO₂ Reduction Catalyzed by Iron Porphyrins. *Chem. Sci.* **2018**, *9*, 2952–2960. [[CrossRef](#)] [[PubMed](#)]
44. Anxolabéhère-Mallart, E.; Costentin, C.; Fournier, M.; Nowak, S.; Robert, M.; Savéant, J.-M. Boron-Capped Tris(glyoximate) Cobalt Clathrochelate as a Precursor for the Electrodeposition of Nanoparticles Catalyzing H₂ Evolution in Water. *J. Am. Chem. Soc.* **2012**, *134*, 6104–6107. [[CrossRef](#)]
45. Lassalle-Kaiser, B.; Zitolo, A.; Fonda, E.; Robert, M.; Anxolabéhère-Mallart, E. In Situ Observation of the Formation and Structure of Hydrogen-Evolving Amorphous Cobalt Electrocatalysts. *ACS Energy Lett.* **2017**, *2*, 2545–2551. [[CrossRef](#)]
46. Nie, W.; Wang, Y.; Zheng, T.; Ibrahim, A.; Xu, Z.; McCrory, C.C.L. Electrocatalytic CO₂ Reduction by Cobalt Bis(pyridyl)monoimine Complexes: Effect of Ligand Flexibility on Catalytic Activity. *ACS Catal.* **2020**, *10*, 4942–4959. [[CrossRef](#)]
47. Sheng, H.; Frei, H. Direct Observation by Rapid-Scan FT-IR Spectroscopy of Two-Electron-Reduced Intermediate of Tetraaza Catalyst [Co^{II}N₄H(MeCN)]²⁺ Converting CO₂ to CO. *J. Am. Chem. Soc.* **2016**, *138*, 9959–9967. [[CrossRef](#)]
48. Kou, Y.; Nabetani, Y.; Masui, D.; Shimada, T.; Takagi, S.; Tachibana, H.; Inoue, H. Direct Detection of Key Reaction Intermediates in Photochemical CO₂ Reduction Sensitized by a Rhenium Bipyridine Complex. *J. Am. Chem. Soc.* **2014**, *136*, 6021–6030. [[CrossRef](#)] [[PubMed](#)]
49. Szalda, D.J.; Fujita, E.; Creutz, C. Cobalt(I), -(II), and -(III) Complexes of a Tetraaza 14-membered Macrocycle, 5,7,7,12,14,14-hexamethyl-1,4,8,11-tetraazacyclotetradeca-4,11-diene (L). Crystal and Molecular Structures of [CoL(CO)]ClO₄, trans-CoLCl₂, and cis-[CoL(CO₃)]ClO₄. *Inorg. Chem.* **1989**, *28*, 1446–1450. [[CrossRef](#)]
50. Schneider, J.; Jia, H.; Muckerman, J.T.; Fujita, E. Thermodynamics and Kinetics of CO₂, CO, and H⁺ Binding to the Metal Centre of CO₂ Reduction catalysts. *Chem. Soc. Rev.* **2012**, *41*, 2036–2051. [[CrossRef](#)]
51. Smieja, J.M.; Benson, E.E.; Kumar, B.; Grice, K.A.; Seu, C.S.; Miller, A.J.M.; Mayer, J.M.; Kubiak, C.P. Kinetic and Structural Studies, Origins of Selectivity, and Interfacial Charge Transfer in the Artificial Photosynthesis of CO. *Proc. Natl. Acad. Sci. USA* **2012**, *109*, 15646–15650. [[CrossRef](#)]
52. Mei, F.; Ou, C.; Wu, G.; Cao, L.; Han, F.; Meng, X.; Li, J.; Li, D.; Liao, Z. Non-heme Iron(ii/iii) Complexes that Model the Reactivity of Lipoygenase with a Redox Switch. *Dalton Trans.* **2010**, *39*, 4267–4269. [[CrossRef](#)] [[PubMed](#)]
53. Zhang, P.; Wang, M.; Gloaguen, F.; Chen, L.; Quentel, F.; Sun, L. Electrocatalytic Hydrogen Evolution from Neutral Water by Molecular Cobalt Tripyridine–diamine Complexes. *Chem. Commun.* **2013**, *49*, 9455–9457. [[CrossRef](#)] [[PubMed](#)]
54. Becke, A.D. A New Mixing of Hartree-Fock and Local Density Functional Theories. *J. Chem. Phys.* **1993**, *98*, 1372–1377. [[CrossRef](#)]
55. Lee, C.; Yang, W.; Parr, R.G. Development of the Colle-Salvetti Correlation-energy Formula into a Functional of the Electron Density. *Phys. Rev. B* **1988**, *37*, 785–789. [[CrossRef](#)]
56. Chen, L.; Guo, Z.; Wei, X.-G.; Gallenkamp, C.; Bonin, J.; Anxolabéhère-Mallart, E.; Lau, K.-C.; Lau, T.-C.; Robert, M. Molecular Catalysis of the Electrochemical and Photochemical Reduction of CO₂ with Earth-Abundant Metal Complexes. Selective Production of CO vs. HCOOH by Switching of the Metal Center. *J. Am. Chem. Soc.* **2015**, *137*, 10918–10921. [[CrossRef](#)]

Disclaimer/Publisher’s Note: The statements, opinions and data contained in all publications are solely those of the individual author(s) and contributor(s) and not of MDPI and/or the editor(s). MDPI and/or the editor(s) disclaim responsibility for any injury to people or property resulting from any ideas, methods, instructions or products referred to in the content.